JACS
JOURNAL OF THE AMERICAN CHEMICAL SOCIETY

pubs.acs.org/JACS

Article

Guest-Controlled Incommensurate Modulation in a Meta-Rigid Metal–Organic Framework Material

Jiangnan Li,[•] Zhengyang Zhou,[•] Xue Han, Xinran Zhang, Yong Yan, Weiyao Li, Gemma L. Smith, Yongqiang Cheng, Laura J. McCormick McPherson, Simon J. Teat, Mark D. Frogley, Svemir Rudić, Anibal J. Ramirez-Cuesta, Alexander J. Blake, Junliang Sun,* Martin Schröder,* and Sihai Yang*

Cite This: *J. Am. Chem. Soc.* 2020, 142, 19189–19197

Read Online

ACCESS | Metrics & More | Article Recommendations | Supporting Information

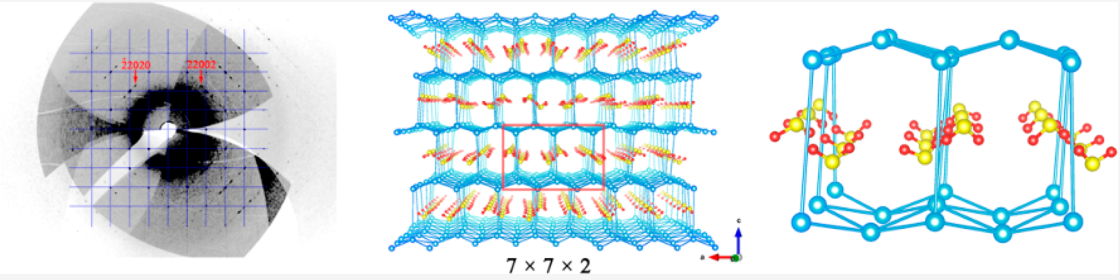

ABSTRACT: Structural transitions of host systems in response to guest binding dominate many chemical processes. We report an unprecedented type of structural flexibility within a meta-rigid material, MFM-520, which exhibits a reversible periodic-to-aperiodic structural transition resulting from a drastic distortion of a [ZnO_4N] node controlled by the specific host–guest interactions. The aperiodic crystal structure of MFM-520 has no three-dimensional (3D) lattice periodicity but shows translational symmetry in higher-dimensional (3 + 2)D space. We have directly visualized the aperiodic state which is induced by incommensurate modulation of the periodic framework of MFM-520·H_2O upon dehydration to give MFM-520. Filling MFM-520 with CO_2 and SO_2 reveals that, while CO_2 has a minimal structural influence, SO_2 can further modulate the structure incommensurately. MFM-520 shows exceptional selectivity for SO_2 under flue-gas desulfurization conditions, and the facile release of captured SO_2 from MFM-520 enabled the conversion to valuable sulfonamide products. MFM-520 can thus be used as a highly efficient capture and delivery system for SO_2.

INTRODUCTION

Metal–organic framework (MOF) materials are synthetic porous materials constructed from bridging metal centers and organic ligands.[1] MOFs can be either rigid[2] or flexible[3] depending upon the metal–ligand coordination combination, framework topology, and organic functionality. Rigid MOFs retain a well-defined framework structure and pore interior against external variables (e.g., temperature, pressure, and guest inclusion), making them useful for the separation and purification of substrates.[2,4] In contrast, flexible MOFs can undergo reversible breathing transitions between typically two well-defined periodic crystal structures. One form is often described as narrow-pored and the other form is described as large-pored, and these two forms therefore show different porosities and properties.[5−10]

Figure 1 illustrates various structural responses to guest binding within a MOF lattice. Breathing and metastable MOFs show two prevailing types of phase transitions, namely, periodic-to-periodic and periodic-to-amorphous. Beyond that, there is also an intriguing class of mesoporous MOFs, allowing the formation of adsorbate superlattices based upon long-range collective adsorbate–adsorbate interactions.[11] The periodic-to-aperiodic transition observed here for MFM-520 represents a new type of framework flexibility in crystalline porous solids. Superspace group theory[12] has been used to describe the commensurate structure of crystalline zeolite SSZ-57[13] in higher-dimensional space, and this has been applied to interpret the incommensurate modulated structures described here.

EXPERIMENTAL SECTION

Synthesis of MFM-520. All reagents were used as received from commercial suppliers without purification. The synthesis of H_4L (4,4′-bipyridine-2,6,2′,6′-tetracarboxylic acid) and $\{[Zn_2(L)\cdot 4H_2O]\}_\infty$

Received: August 15, 2020
Published: October 30, 2020

https://dx.doi.org/10.1021/jacs.0c08794
J. Am. Chem. Soc. 2020, 142, 19189–19197

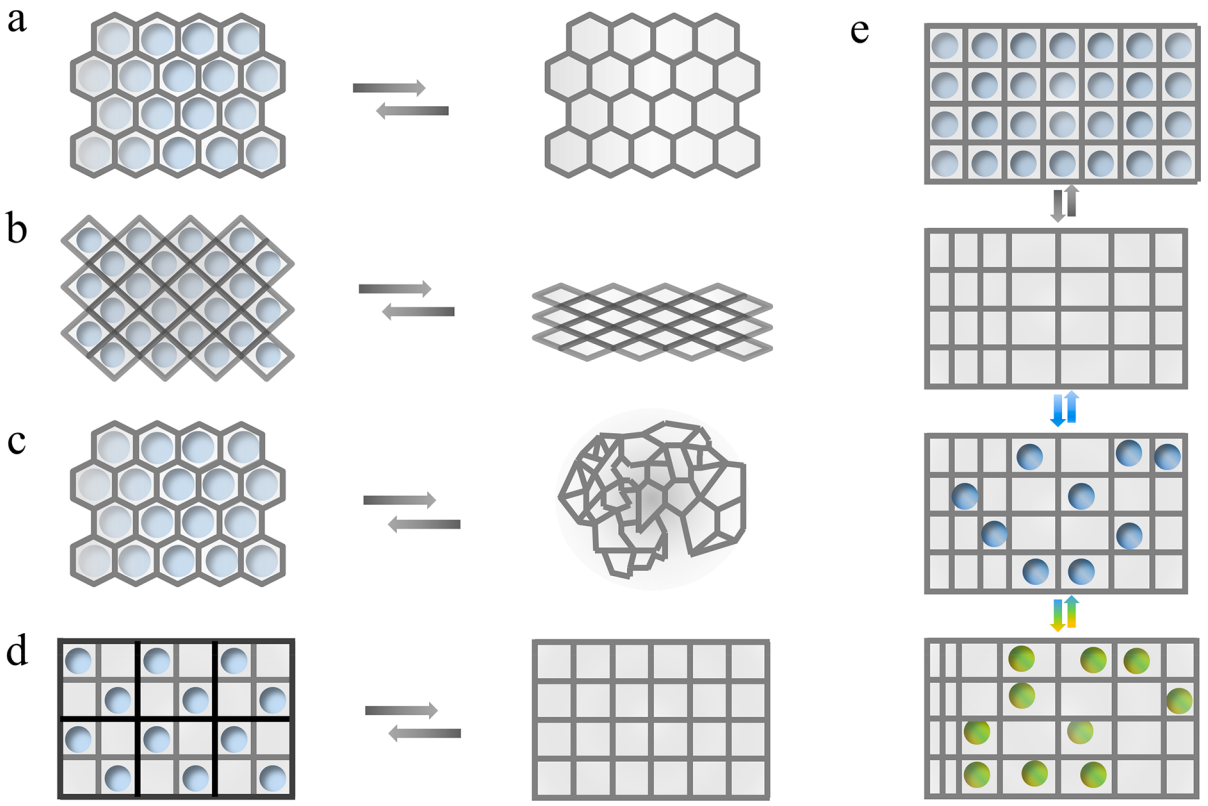

Figure 1. Representation of structural transitions in various types of MOFs upon guest inclusion and removal. MOFs and guest molecules are shown by solid lines and shaded spheres, respectively. (a) Rigid MOF showing full retention of the framework structure on gas adsorption and desorption. (b) Flexible MOF showing reversible framework breathing between a narrow-pore phase and a large-pore phase. (c) Metastable MOF showing irreversible framework amorphization. (d) Mesoporous MOF showing the formation of superlattices of adsorbates. (e) Meta-rigid MOF, MFM-520, showing reversible incommensurate modulation of the framework structure on going from (top to bottom) MFM-520·H_2O (top) to MFM-520 to MFM-520·CO_2 (CO_2 represented by blue spheres) to MFM-520·SO_2 (SO_2 represented by green spheres) (bottom).

(MFM-520·H_2O) was carried out using previously reported methods.[14]

***In Situ* Synchrotron Single-Crystal X-ray Diffraction and Structural Characterization.** *In situ* synchrotron X-ray single-crystal diffraction data were collected on beamline 11.3.1 of the Advanced Light Source using monochromated radiation [λ = 0.7749(1) Å]. After data collection for as-synthesized sample MFM-520·H_2O, the same single crystal (0.10 × 0.05 × 0.05 mm^3) was placed in a capillary gas handling cell and evacuated *in situ* under dynamic vacuum and a stream of N_2 at 340 K centered on the capillary for 4 h. The single-crystal diffraction data of dehydrated MFM-520 were collected at 290 K. Upon loading of CO_2 into MFM-520 at 1.0 bar and 290 K, three diffraction data sets were collected at 270 K to examine the possible dynamic behavior of the structural relaxation (i.e., adsorbate−adsorbent equilibrium and change in the modulation vector). The single crystal was then reactivated under vacuum and heating to remove all adsorbed gases. The *in situ* single-crystal diffraction data for SO_2-loaded MFM-520 were collected using the same method as for the CO_2-loaded sample.

The influence of temperature on the periodic-to-aperiodic phase transition was monitored by collecting *in situ* single-crystal diffraction data for dehydrated MFM-520 at 180−350 K on a Rigaku Oxford XtaLAB diffractometer using Mo-$K\alpha$ radiation. No change in the modulation vectors of MFM-520 was observed between 180 and 350 K (Table S2), confirming the negligible impact of temperature on the modulation vector of MFM-520.

To examine the reversibility of the periodic-to-aperiodic phase transition observed in MFM-520, a single crystal of rehydrated MFM-520·H_2O, formed by the treatment of dehydrated MFM-520 with water, was studied by single-crystal diffraction at 180 K. This experiment confirms the absence of satellite reflections of the rehydrated sample (Figure S6).

In the (3 + 2)D incommensurately modulated structure, each parameter of modulation can be expanded as a Fourier series using eq 1:

$$p_m^{\mu}(x_4, x_5) = \sum_n \sum_m [p_{snm}^{\mu} \sin(2\pi n x_4 + 2\pi m x_5) + p_{cnm}^{\mu} \cos(2\pi n x_4 + 2\pi m x_5)] \quad (1)$$

where $x_4 = \mathbf{q}_1\mathbf{r}^{\mu} + t$, $x_5 = \mathbf{q}_2\mathbf{r}^{\mu} + u$, and t and u are initial phases in the range of 0 to 1. The real structural parameters can be expressed as eq 2:

$$p_{real}^{\mu}(x_4, x_5) = p_m^{\mu}(x_4, x_5) + p_{ave}^{\mu} \quad (2)$$

The average structure parameters p_{ave}^{μ} were determined by direct methods and least-squares refinements, and the modulations were refined globally using free variables. All non-hydrogen atoms were refined anisotropically, and hydrogen atoms were placed using a riding model. Given the complexity of the structure, soft constraints on the bond length/angle to both host and guest were applied in the final stage of refinement. All refinements of the crystal structures were performed on the JANA2006 software platform.[15]

Gas Adsorption Isotherms. Gravimetric sorption isotherms for N_2, CO_2, SO_2, CH_4, CO, and O_2 were recorded at various temperatures on a Hiden Isochema IGA-003 system under high vacuum (10^{-10} bar) produced by a turbo pumping system. Temperatures were maintained using a programmed water bath. Ultra-pure research grade gases (99.999%) were purchased from BOC or Air Liquide. In a typical gas adsorption experiment, 50 mg of acetone-exchanged MFM-520 was loaded into the IGA system and activated at 393 K under dynamic high vacuum (10^{-10} bar) for 1 day

https://dx.doi.org/10.1021/jacs.0c08794
J. Am. Chem. Soc. 2020, 142, 19189−19197

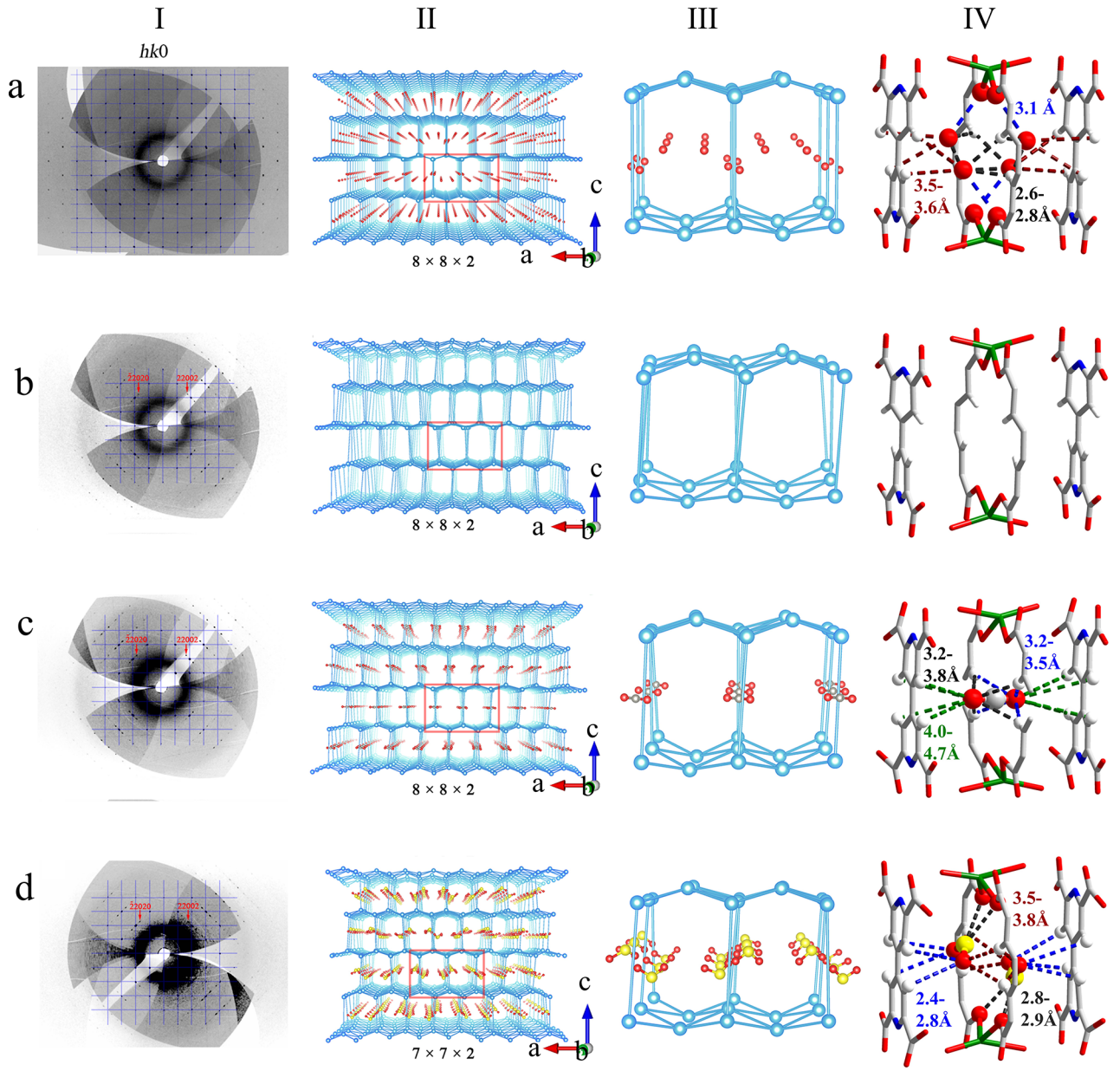

Figure 2. Column I: views of *in situ* synchrotron X-ray diffraction images of the *hk*0 plane. Column II: views of the corresponding crystal structures of MFM-520 as a function of guest inclusion/removal. 8 × 8 × 2 means the unit cell of the modulated structure is 8 times that of the average structure along the *a* and *b* axes and 2 times along the *c* axis; 7 × 7 × 2 means the unit cell of the modulated structure is 7 times that of the average structure along the *a* and *b* axes and 2 times along the *c* axis. Column III: details of the structure shown in the red box in column II. Column IV: molecular details of host−guest interactions. The MOF framework, zinc, oxygen, carbon, and sulfur are shown in blue, green, red, gray, and yellow, respectively. Bond distances are shown in Å. (a) MFM-520·H_2O, (b) MFM-520, (c) MFM-520·CO_2, and (d) MFM-520·SO_2. A comparison of all *in situ* synchrotron X-ray diffraction images of the *hk*0.5 and *hk*1 planes is shown in Figure S5. The reflection conditions of MFM-520·H_2O are 00*l*: *l* = 2 × integer and *h*00: *h* = 2 × integer. According to superspace group theory,[12] there is a supercentered setting with $\mathbf{a}_s = \mathbf{a}$, $\mathbf{b}_s = \mathbf{b}$, $\mathbf{c}_s = 2\mathbf{c}$, $\mathbf{Q}_1 = \alpha(\mathbf{a}_s^* + \mathbf{b}_s^*)$, and $\mathbf{Q}_2 = \alpha(-\mathbf{a}_s^* + \mathbf{b}_s^*)$, which is equivalent to the basic setting **a**, **b**, **c**, $\mathbf{q}_1 = \alpha(\mathbf{a}^* + \mathbf{b}^*) + 0.5\mathbf{c}^*$, and $\mathbf{q}_2 = \alpha(-\mathbf{a}^* + \mathbf{b}^*) + 0.5\mathbf{c}^*$. Because the tables of (3 + 2)D superspace groups[19] provide only reflection conditions with supercenterd settings, we transformed the basic setting to supercentered settings to determine the reflection conditions. With the supercentered setting, the *hk*0, *hk*0.5, and *hk*1 planes are transformed to *HK*0, *HK*1, and *HK*2, respectively (Figure S5). The reflection conditions of MFM-520, MFM-520·CO_2, and MFM-520·SO_2 are *HKLMN*: *L* + *M* + *N* = 2 × integer, *HK*0*MN*: *M* = 2 × integer, *HHLM*0: *L* = 2 × integer, $H\bar{H}L0N$: *N* = 2 × integer, *H*0*LM*$\bar{M}$: 2*H* + *L* + 2M = 4 × integer, and 0*KLMM*: 2*K* + *L* + 2M = 4 × integer, corresponding to (3 + 2)D superspace group 136.2.69.10, adopting the symbol $P4_2/mnm(\alpha, \alpha, 1/2)$ 00qs$(-\alpha, \alpha, 1/2)$0sq0 with basic settings.

to give fully desolvated MFM-520. BET surface areas and porosity data were obtained from N_2 isotherm data at 77 K.

Gas Separation by Breakthrough Experiments. In the breakthrough experiments, the flow rate of the entering gas mixture was maintained at 50 mL min^{-1}, and the gas concentration, *C*, of SO_2, CO_2, and N_2 at the outlet was determined by mass spectrometry and compared with the corresponding inlet concentration C_0, where C/C_0 = 1 indicates complete breakthrough. Breakthrough separation of SO_2/CO_2 was conducted using a mixture containing SO_2 (2500 ppm) and 15% CO_2 (v/v) diluted in He through a fixed bed packed with MFM-520 at 298 and 318 K and 1 bar at a flow rate of 50 mL min^{-1}.

https://dx.doi.org/10.1021/jacs.0c08794
J. Am. Chem. Soc. 2020, 142, 19189−19197

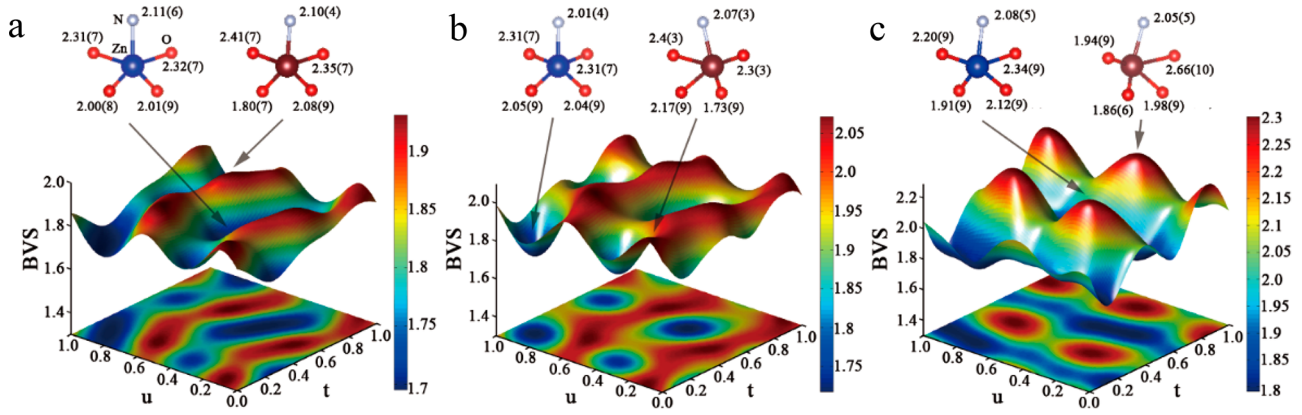

Figure 3. Maps of the bond valence sum (BVS) analyses of the oxidation state of Zn(II) centers as a function of the modulation vector u and t in (a) MFM-520, (b) MFM-520·CO_2, and (c) MFM-520·SO_2. The coordination geometries of the [ZnO_4N] polyhedra for the lowest and highest (highlighted in blue and brown, respectively) BVS analysis maps for MFM-520, MFM-520·CO_2, and MFM-520·SO_2 are illustrated above the contour maps. Bond distances are in Å. BVS parameters R_{ij}(Zn−O), b_0(Zn−O), R_{ij}(Zn−N), and b_0(Zn−N) are 1.704, 0.37, 1.72, and 0.37 Å, respectively. MFM-520·H_2O has a periodic structure and shows no modulation by BVS analysis; the formal oxidation state of all Zn(II) centers in MFM-520·H_2O is 1.974(14).

The final results have been converted to dimensionless plots as shown in Figure 4.

The fixed bed of MFM-520 for the adsorptive removal of low concentrations of SO_2 under wet conditions was first exposed to a flow of 1.5% H_2O in He until the breakthrough of water. A stream of 0.25% SO_2 (i.e., 2500 ppm) diluted in He was then flowed through the packed bed of MFM-520 (approximately 1 g) at a total flow rate of 50 mL min^{-1} at 298 K and 1.0 bar. Dimensionless breakthrough plots were calculated with the following parameters: bed diameter, d, (7 mm); bed length, L, (120 mm); bed volume (5.0 mL); sample mass (1.0 g); sample framework density (1.55 g/cm^3); and flow rate (50 mL/min). The sample occupied a volume of 0.65 mL (assuming 100% purity and no framework collapse), and thus the fractional porosity of the fixed bed, ε, was calculated to be 0.87. The superficial gas velocity, u, at the entrance of the bed corresponded to 0.22 m/s, and the characteristic contact time between the gas and the sample of MFM-520 corresponded to $\varepsilon L/u$ = 4.82 s. The dimensionless time, τ, was obtained by dividing the actual time, t, by the contact time between the gas and the MFM-520 sample, $\varepsilon L/u$ (i.e., $\tau = tu/\varepsilon L$).

Inelastic Neutron Scattering (INS) Experiments. INS spectra were recorded on the TOSCA spectrometer at the ISIS Facility at the STFC Rutherford Appleton Laboratory. TOSCA is an indirect geometry instrument that provides a wide spectral range (−25 to 4000 cm^{-1}) with resolution optimized in the 50−2000 cm^{-1} range. In this region, TOSCA has a resolution of 1.25% of the energy transfer. The instrument is composed of 130 ^{3}He detectors in forward and backscattering geometries located 17 m downstream from a 300 K Gd poisoned water moderator. A temperature of 10 ± 0.2 K was maintained during data collection by two He closed-cycle refrigerators with 30 mbar He as an exchange gas.

A sample of MFM-520 was activated at 120 °C and 1 × 10^{-7} mbar for 1 day and then placed into an 11-mm-diameter vanadium sample can, which was loaded into a helium closed-cycle refrigerator (CCR) cryostat and cooled to 10 K for data collection. Defined amounts of CO_2 and SO_2 were introduced by warming the sample to 290 K, and the gas was dosed volumetrically from a calibrated volume. The gas-loaded sample was then cooled to 10 K over a period of 2 h to ensure good mobility of adsorbed gases within the crystalline MFM-520. The sample was retained at 10 K for an additional 30 min before data collection to ensure thermal equilibrium.

Density Functional Theory (DFT) Calculations. DFT calculations were performed using CASTEP (version 19.11).[16] The generalized gradient approximation (GGA) as implemented by Perdew−Burke−Ernzerhof (PBE) was used to describe the exchange-correlation interactions. On-the-fly norm-conserving pseudopotentials were employed to account for the effects of core electrons with the default energy cutoff (~870 eV) for the plane-wave basis. The unit cell configuration determined by XRD was used as the initial structure for the simulations. The atomic coordinates of the guest molecules were first relaxed by molecular dynamics at 300 K for 10 ps to find the optimal binding sites that are not constrained by symmetry (the MOF structure was fixed during this relaxation). The final configurations (including both the MOF and the guest molecules) were further relaxed using the conjugate gradient method to allow minimization of the potential energy and the interatomic forces. The energy tolerance for the electronic structure calculations was 5 × 10^{-10} eV, and the energy tolerance for ionic relaxation was 5 × 10^{-9} eV. The tolerance for the interatomic forces was 1 meV/Å. After convergence, the dynamic matrix was obtained using the linear response method, from which the phonon frequencies and vibrational modes were calculated. The electronic structure calculations were performed on a 3 × 3 × 1 Monkhorst−Pack mesh, and the dynamic matrix was calculated directly on the same mesh and then interpolated on a 7 × 7 × 3 Monkhorst−Pack mesh. The IR intensities were directly computed with CASTEP.[16] The OClimax software[17] was used to convert the DFT-calculated phonon results to the simulated INS spectra.

Conversion of Captured SO_2. MFM-520 was activated at 393 K under vacuum overnight. The sample was cooled, and MFM-520 was dosed with SO_2 for 1 h to reach adsorption equilibrium. Morpholin-4-amine (128.0 mg, 1.25 mmol) and SO_2@MFM-520 (357 mg, equivalent to 1.18 mmol of SO_2) were suspended in CH_3CN (3 mL) and stirred for 1 h. 4-Methoxy-aryldiazonium tetrafluoroborate (55.0 mg, 0.25 mmol) in CH_3CN (1 mL) was added dropwise to the above suspension, and the mixture was stirred at room temperature for 1 h. The mixture was filtered, and the filtrate was evaporated. NMR spectroscopy and preparative thin layer chromatography (TLC) were used to quantify the conversion of 4-methoxy-aryldiazonium tetrafluoroborate and the yield of the sulfonamide. Benzenaldehyde was used as an internal standard.

RESULTS AND DISCUSSION

MFM-520·H_2O, [Zn_2(L)]·H_2O (H_4L= 4,4-bipyridyl-3,3′,5,5′-tetracarboxylic acid), adopts a 3D open-framework structure comprising square-based pyramidal five-coordinate Zn(II) centers bridged by the tetracarboxylate linker[14] (Figure S1). Each Zn(II) center binds to the N(pyridyl)-donor of L^{4-} along the c axis, and four bridging carboxylates propagate the structure along the diagonals of the ab plane, thus defining an unusual and rigid **sqp** topology.[18] MFM-520·H_2O exhibits bow-tie-shaped pores with dimensions of 6.6 × 4.0 $Å^2$ which

https://dx.doi.org/10.1021/jacs.0c08794
J. Am. Chem. Soc. 2020, 142, 19189−19197

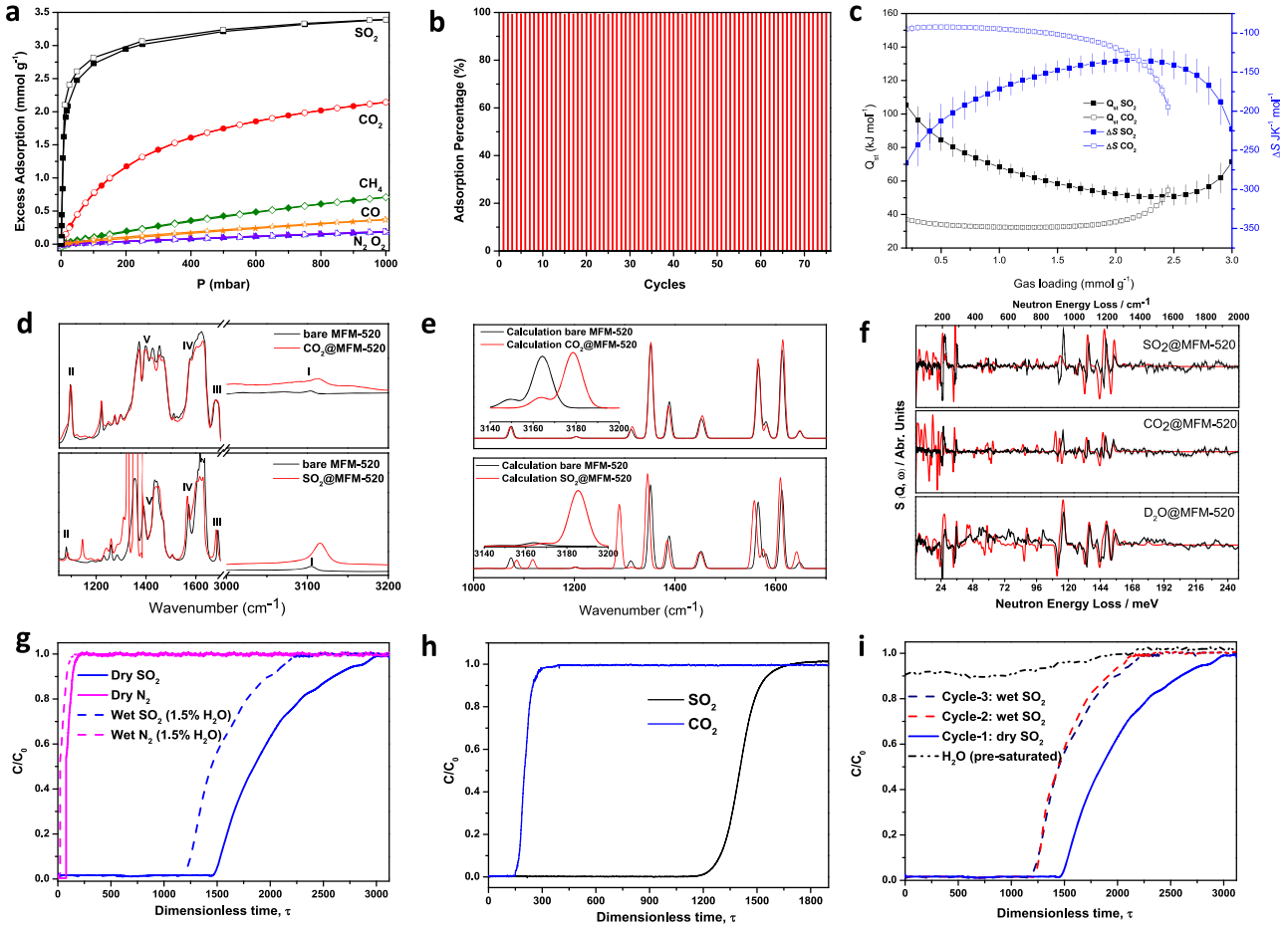

Figure 4. Gas adsorption, selectivity, stability, thermodynamic, spectroscopy, and dynamic separation data. (a) Adsorption isotherms for SO_2, CO_2, CH_4, CO, O_2, and N_2 in MFM-520 at 298 K (solid symbols, adsorption; open symbols, desorption). (b) Comparison of the SO_2 adsorption capacity of MFM-520 over 75 cycles at 298 K. (c) Variation of isosteric heats of adsorption (Q_{st}) and adsorption entropy (ΔS) for SO_2 and CO_2 uptake in MFM-520. (d) Comparison of experimental FTIR spectra for bare and CO_2- and SO_2-loaded MFM-520. (e) Comparison of DFT-calculated FTIR spectra for bare and CO_2- and SO_2-loaded MFM-520. (f) Comparison of the difference plots for experimental and DFT-calculated INS spectra of D_2O-, CO_2-, and SO_2-loaded MFM-520 (black, experiment; red, calculation). The discrepancies, particularly for the lattice modes at low energy (<200 cm^{-1}), are due to the limitation that DFT simulations can be conducted only on average unit cells, which does not take the incommensurate modulation into consideration. (g) Dimensionless breakthrough plots for SO_2/N_2 mixtures under dry (solid lines) and humid (dashed lines) conditions. Dry conditions: 2500 ppm SO_2, 99.75% N_2, total flow rate 50 mL min^{-1}. Wet conditions: 1.5% H_2O, 2500 ppm SO_2, 98.25% N_2, total flow rate 50 mL min^{-1}. (h) Dimensionless breakthrough plots for SO_2/CO_2 mixtures at 298 K (15% CO_2, 2500 ppm SO_2, 84.75% He, total flow rate 50 mL min^{-1}). (i) Dimensionless breakthrough plots for cyclic SO_2 adsorption under both dry and humid conditions. Dry conditions: 2500 ppm SO_2, 99.75% He, total flow rate 50 mL min^{-1}. Wet conditions: 1.5% H_2O, 2500 ppm SO_2, 98.25% He, total flow rate 50 mL min^{-1}. For experiments under humid conditions, the bed was first exposed to a flow of 1.5% H_2O in He until the breakthrough of water.

are filled with guest water molecules which assemble into 1D helical chains along the [110] direction. These chains are stabilized by strong intermolecular hydrogen bonds [$O_w\cdots O_w$ = 2.934(11), 2.887(11) Å] (Figure S2). The water molecules are also hydrogen bonded to the framework oxygen center of the ligand [$O_w\cdots$O2 = 3.064(9) Å] (Figure 2a-IV), inducing the overall structure to crystallize in tetragonal space group $P4_22_12$ [$a = b$ = 7.0211(6), c = 19.9558(15) Å]. These complementary host−guest and guest−guest hydrogen bonds stabilize the periodic structure of MFM-520·H_2O and restrict its freedom for structural relaxation.

On heating MFM-520·H_2O at 340 K under dynamic vacuum, additional satellite reflections appear at positions defined by modulation vectors 0.1240(3)(**a*** + **b***) + 0.5**c*** and 0.1240(3)(−**a*** + **b***) + 0.5**c*** on the plane diffraction patterns (Figure 2b-I), indicating that an intriguing structural transition has occurred. The loss of guest water molecules removes the stabilizing network of hydrogen bonding and thus creates voids and freedom for the [ZnO_4N] polyhedra to relax. Bond distances Zn−N1, Zn−O1, and Zn−O2 in MFM-520·H_2O [2.002(6), 2.214(6), and 1.959(5) Å, respectively] change with the loss of water and lie in ranges of 2.07−2.12, 2.25−2.58, and 1.79−2.11 Å, respectively, for dehydrated MFM-520. This is accompanied by the modulation of the electron density at the Zn(II) center with the formal oxidation state ranging from 1.70(10) to 1.93(10) in MFM-520 as determined by bond valence sum (BVS) calculations[20] for the different Zn(II) centers (Figure 3a). In contrast, those in MFM-520·H_2O have the same charge of 1.974(14).

The resulting structure of dehydrated MFM-520 is aperiodic in 3D space but periodic in (3 + 2)D space, and the two modulated vectors (q_1 and q_2) are projections of the additional two dimensions along the three directions of 3D reciprocal space. Importantly, all satellite reflections of dehydrated MFM-520 disappear on rehydration to MFM-520·H_2O, demonstrating the reversibility of this periodic-to-aperiodic phase

https://dx.doi.org/10.1021/jacs.0c08794
J. Am. Chem. Soc. 2020, 142, 19189−19197

transition (Figure S6). No change was observed in the modulation vectors for dehydrated MFM-520 between 180 and 350 K (Table S2). Interestingly, for the periodic-to-aperiodic phase transitions in inorganic materials, metal alloys, and organic compounds, which are induced by changes in temperature and electric and magnetic fields,[21−24] the periodic-to-aperiodic transition observed in MFM-520 is controlled by host−guest interactions, representing the first example of such a phenomenon for an inorganic−organic hybrid material or porous solid.

Dehydrated MFM-520 displays a BET surface area of 313 $m^2\ g^{-1}$ and a pore volume of 0.146 $cm^3\ g^{-1}$,[14] and single-component adsorption isotherms for SO_2, CO_2, CH_4, CO, O_2, and N_2 in MFM-520 have been recorded at 273−318 K up to 1.0 bar (Figure 4a, Figures S9−S12). The excess adsorption uptake of SO_2 at 298 K and 1.0 bar is 3.38 mmol g^{-1}, which is higher than those of CO_2, CH_4, CO, O_2, and N_2 (0.77, 0.71, 0.36, 0.19, and 0.18 mmol g^{-1}, respectively). More significantly, at low pressure (e.g., 0.01 bar, 298 K), where all other gases show negligible uptakes (0.09 mmol g^{-1} for CO_2; <0.01 mmol g^{-1} for CH_4, CO, O_2, and N_2), MFM-520 displays a notably higher isothermal uptake of SO_2 (1.66 mmol g^{-1}), accompanied by fast adsorption kinetics typically within minutes (Figures S13 and S14). The static SO_2 uptake of MFM-520 is comparable to those of the best-behaving sorbents but is lower than the dynamic SO_2 uptake of SIFSIX-2-Cu-i,[25] which possesses very narrow pores (Table S3). Often, there is a trade-off between high adsorption at low pressure and difficulties in the complete regeneration of narrow-pored MOFs. Facile regeneration of the SO_2-saturated MFM-520 can be readily achieved solely via a pressure swing, and no loss of SO_2 adsorption capacity or crystallinity of MFM-520 was observed after 75 cycles of SO_2 adsorption−desorption (Figure 4b).

Further analysis of the adsorption thermodynamics of MFM-520 reveals that the isosteric heat of adsorption (Q_{st}) for CO_2 is 32−48 kJ mol^{-1} and the entropy of adsorption (ΔS) decreases steadily with increasing surface coverage, consistent with the expected ordering of adsorbed CO_2 molecules in MFM-520. In comparison, Q_{st} for SO_2 adsorption reaches ~120 kJ mol^{-1} at low surface coverage and decreases gradually to 60 kJ mol^{-1} with increasing loading of SO_2. The calculated value of Q_{st} is consistent with the calorimetric measurements of 43 and 96 kJ mol^{-1} for CO_2 and SO_2 adsorption, respectively (Figures S15 and S16). The higher value of Q_{st} for SO_2 uptake is consistent with the expected stronger interaction between the framework and SO_2 compared with CO_2. However, the ΔS for SO_2 adsorption increases steadily from an initial −260 to −135 J K^{-1} mol^{-1} with increasing loading of SO_2. This observation is opposite to the prevailing understanding of gas adsorption in porous materials, where ordering of the gas molecules results in a decrease in ΔS on gas loading[26−28] and implies increasing disorder of the system on SO_2 loading in MFM-520.

We sought to understand the origin of this intriguing pattern in ΔS and have determined the host−guest structures of CO_2- and SO_2-loaded MFM-520 by *in situ* synchrotron X-ray single-crystal diffraction (Table S1). On loading CO_2 into MFM-520 at 270 K and 1.0 bar, adsorbed CO_2 molecules are clearly observed in the pores, corresponding to a crystallographic uptake of 2.18 mmol g^{-1}, in excellent agreement with the isotherm uptake (2.14 mmol g^{-1}). All guest CO_2 molecules in MFM-520·CO_2 were found to be incommensurate (Figure 2c). Thus, instead of showing a constant distance between adjacent CO_2 molecules, the intermolecular distances range from *ca.* 6.6 to 7.4 Å (Figure S3), indicating no apparent interaction between adjacent CO_2 molecules. The distances between CO_2 and phenyl rings (C1···pyridyl ring) and between CO_2 and aromatic −CH groups (O3···H1C2−C2) are longer than 3.0 Å (Figure 2c-IV), suggesting only very weak supramolecular interactions between the host framework and CO_2. Therefore, MFM-520 experiences no change in structure upon CO_2 adsorption, and both the oxidation state of Zn(II) centers [ranging from 1.73(9) to 2.07(9)] and the geometry of [ZnO_4N] nodes in MFM-520·CO_2 [Zn−N1, Zn−O1, and Zn−O2 bond distances ranging between approximately 2.00 and 2.07, 2.20 and 2.50, and 1.72 and 2.25 Å, respectively] are similar to those of bare MFM-520 (Figure 3b, Figures S7 and S8). Thus, the two modulation vectors [0.1243(3)(**a*** + **b***) + 0.5**c*** and 0.1243(3)(−**a*** + **b***) + 0.5**c***] in MFM-520 remain upon adsorption of CO_2.

Upon loading of SO_2 into MFM-520 at 270 K and 1.0 bar, a crystallographic uptake of SO_2 of 3.16 mmol g^{-1} is observed, in excellent agreement with the isotherm uptake (3.38 mmol g^{-1}). Since the occupancy of adsorbed SO_2 molecules is 0.359(13) in the refined structural model of MFM-520·SO_2, half of the closely contacted SO_2 molecules (*ca.* 1.7 to 1.9 Å) were removed, and the remaining SO_2 molecules have an intermolecular distance of *ca.* 3.5 Å (Figure S4), which is shorter than that in MFM-520·CO_2, suggesting stronger guest−guest interactions between adsorbed SO_2 molecules.

On the other hand, strong MOF−SO_2 binding is indicated by the short distances between SO_2 and aromatic −CH groups (O3···H1C2−C2: *ca.* 2.33 to 2.75 Å) and between SO_2 and [ZnO_4N] polyhedra (S1···O2: *ca.* 2.78 to 3.34 Å) (Figure 2d-IV, Figures S7 and S8). As a result, the structure of MFM-520 is heavily affected by adsorbed SO_2 molecules. The ranges of bond distances Zn−N1, Zn−O1, and Zn−O2 in MFM-520·SO_2 vary from 1.97 to 2.14, 1.92 to 2.73, and 1.75 to 2.19 Å, respectively, much wider than those observed in MFM-520 and MFM-520·CO_2. The oxidation state of the Zn(II) centers also shows a greater range between 1.79(9) and 2.29(9) (Figure 3c) compared with that in MFM-520 and MFM-520·CO_2. In MFM-520·SO_2, the modulation vectors become 0.1407(6)(**a*** + **b***) + 0.5**c*** and 0.1407(6)(−**a*** + **b***) + 0.5**c***, demonstrating a unique incommensurately ordered dynamic equilibrium for SO_2 adsorption. Interestingly, before reaching this equilibrium state, we also identified a transient structure of MFM-520·SO_2 with a corresponding crystallographic SO_2 uptake of 0.532 mmol g^{-1} that has intermediate modulation vectors of 0.1331(4)(**a*** + **b***) + 0.5**c*** and 0.1331(4)(−**a*** + **b***) + 0.5**c*** (Table S1). The change in the incommensurate modulation of MFM-520 induced by the uptake of SO_2 is a dynamic process as a function of diffusion and the settling of SO_2 molecules within the pores of the MOF. This result rationalizes the unusual increase in ΔS on SO_2 loading and confirms that it emanates from a subtle increase in the structural flexibility of meta-rigid MFM-520 upon SO_2 adsorption.

Overall, the incommensurate modulated structure reported here will stimulate a reassessment of a wider range of host−guest systems with unusual adsorption behavior[29,30] and encourage the search for new structural flexibility in other MOFs and porous solids that otherwise may be regarded as entirely rigid.

https://dx.doi.org/10.1021/jacs.0c08794
J. Am. Chem. Soc. 2020, 142, 19189−19197

The binding dynamics and effects on the structural relaxation of MFM-520 have been analyzed further using *in situ* synchrotron infrared microspectroscopy, inelastic neutron scattering (INS), and DFT modeling (Figure 4d–f and Figures S19–S30). Dehydrated MFM-520 has a number of characteristic peaks at 3104, 1080, 1689, 1571, and 1390 cm^{-1} (denoted as I, II, III, IV, and V), which are assigned based upon DFT modeling to the stretching (I) and bending (II) modes of the aromatic C–H groups on the pyridyl ring and the symmetric stretching (III) and asymmetric stretching (IV) modes of C–O and the bending (V) mode of C–H groups, respectively. On dosing CO_2 (0–1 bar), peak I shows a blue shift (Δ = 9 cm^{-1}) to 3113 cm^{-1}, indicating a stiffening of the framework as a result of the binding of CO_2 molecules to –CH groups. No notable changes occur in peaks II–V on CO_2 loading, consistent with the very weak MOF–CO_2 interactions. Upon loading SO_2, a larger blue shift of 12 cm^{-1} is observed for peak I, accompanied by near-depletion of this band on increasing SO_2 loading, demonstrating a stronger –CH···O=S=O supramolecular interaction. Furthermore, distinct red shifts of peaks III and IV (C–O, carboxyl) to 1682 and 1566 cm^{-1} (Δ = 6 and 5 cm^{-1}, respectively) and peak V (C–H, pyridyl ring) to 1385 cm^{-1} (Δ = 5 cm^{-1}) are observed, entirely consistent with the presence of structural distortion as observed in crystallographic studies and DFT-calculated IR spectra (Figure 4e). Difference INS spectra recorded (Figure 4f) between bare and CO_2-, SO_2-, and D_2O-loaded MFM-520 reveal shifts of peaks associated with deformation and twisting modes of the pyridyl rings at low frequencies (200–300 cm^{-1}) as well as C–H bending modes at higher frequencies (900–1300 cm^{-1}), as confirmed by DFT modeling. SO_2 and D_2O both display notably stronger interactions with MFM-520 than CO_2, again consistent with the crystallographic studies.

Unlike conventional once-through FGD (flue gas desulfurization) methods where SO_2 permanently binds to sorbent materials to form solid inorganic waste, the SO_2 captured by MFM-520 remains available to undergo chemical transformation to valuable products.[31,32] A proof-of-concept experiment was thus conducted by coupling 4-methoxyl-aryldiazonium tetrafluoroborates and hydrazine in a solution containing a suspension of MFM-520·SO_2 to synthesize aryl *N*-aminosulfonamides (Scheme 1).[33] A nearly quantitative

Scheme 1. Conversion of Captured SO_2 in MFM-520

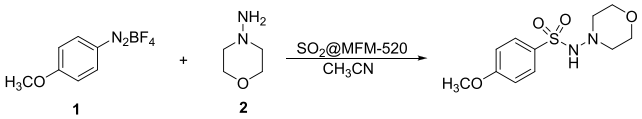

conversion of 4-methoxyl-aryldiazonium tetrafluoroborates and an 80% yield of the sulfonamide were achieved. Immobilization and then release of SO_2 using a stable MOF can thus be used to drive organic reactions effectively, removing the high risk of the large-scale use of caustic and toxic SO_2. In line with the observed structural stability of MFM-520, we have confirmed its reusability for three cycles to produce sulfonamide (Table S6). Thus, MFM-520 represents a stable and efficient platform for the capture, storage, and conversion of SO_2.

CONCLUSIONS

The metal–organic framework material MFM-520 exhibits a reversible periodic-to-aperiodic structural transition. The aperiodic crystal structure of MFM-520 has no three-dimensional (3D) lattice periodicity but shows translational symmetry in higher-dimensional (3 + 2)D space. Filling of MFM-520 with CO_2 and SO_2 reveals that while CO_2 has a minimal structural influence, SO_2 can further modulate the structure incommensurately. In addition, MFM-520 shows high selectivity for SO_2 under flue gas desulfurization conditions, and the facile release of captured SO_2 from MFM-520 can be used as an SO_2 delivery system for subsequent reactivity.

ASSOCIATED CONTENT

Supporting Information

The Supporting Information is available free of charge at https://pubs.acs.org/doi/10.1021/jacs.0c08794.

Additional experimental details, diffraction data, views of crystal structures, INS and IR spectroscopy, adsorption isotherms, and IAST selectivity (PDF)

Crystal data for MFM-520·H_2O (CIF)

Crystal data for MFM-520 (CIF)

Crystal data for MFM-520·CO_2 (CIF)

Crystal data for MFM-520·SO_2 intermediate (CIF)

Crystal data for MFM-520·SO_2 (CIF)

AUTHOR INFORMATION

Corresponding Authors

Junliang Sun – *BNLMS, College of Chemistry & Molecular Engineering, Peking University, Beijing 100871, China;* orcid.org/0000-0003-4074-0962; Email: junliang.sun@pku.edu.cn

Martin Schröder – *Department of Chemistry, University of Manchester, Manchester M13 9PL, U.K.;* orcid.org/0000-0001-6992-0700; Email: M.Schroder@manchester.ac.uk

Sihai Yang – *Department of Chemistry, University of Manchester, Manchester M13 9PL, U.K.;* orcid.org/0000-0002-1111-9272; Email: Sihai.Yang@manchester.ac.uk

Authors

Jiangnan Li – *Department of Chemistry, University of Manchester, Manchester M13 9PL, U.K.*

Zhengyang Zhou – *BNLMS, College of Chemistry & Molecular Engineering, Peking University, Beijing 100871, China*

Xue Han – *Department of Chemistry, University of Manchester, Manchester M13 9PL, U.K.*

Xinran Zhang – *Department of Chemistry, University of Manchester, Manchester M13 9PL, U.K.*

Yong Yan – *Department of Chemistry, University of Manchester, Manchester M13 9PL, U.K.;* orcid.org/0000-0002-7926-3959

Weiyao Li – *Department of Chemistry, University of Manchester, Manchester M13 9PL, U.K.*

Gemma L. Smith – *Department of Chemistry, University of Manchester, Manchester M13 9PL, U.K.*

Yongqiang Cheng – *Neutron Scattering Division, Neutron Sciences Directorate, Oak Ridge National Laboratory, Oak Ridge, Tennessee 37831, United States;* orcid.org/0000-0002-3263-4812

https://dx.doi.org/10.1021/jacs.0c08794
J. Am. Chem. Soc. 2020, 142, 19189–19197

Laura J. McCormick McPherson − *Advanced Light Source, Lawrence Berkeley National Laboratory, Berkeley, California 94720, United States*
Simon J. Teat − *Advanced Light Source, Lawrence Berkeley National Laboratory, Berkeley, California 94720, United States*
Mark D. Frogley − *Diamond Light Source, Harwell Science Campus, Oxfordshire OX11 0DE, U.K.*
Svemir Rudić − *ISIS Facility, STFC Rutherford Appleton Laboratory, Chilton, Oxfordshire OX11 0QX, U.K.*
Anibal J. Ramirez-Cuesta − *Neutron Scattering Division, Neutron Sciences Directorate, Oak Ridge National Laboratory, Oak Ridge, Tennessee 37831, United States;* orcid.org/0000-0003-1231-0068
Alexander J. Blake − *School of Chemistry, University of Nottingham, Nottingham NG7 2RD, U.K.*

Complete contact information is available at: https://pubs.acs.org/10.1021/jacs.0c08794

Author Contributions

•J.L. and Z.Z. contributed equally.

Notes

The authors declare no competing financial interest.

■ ACKNOWLEDGMENTS

We thank the EPSRC (EP/I011870), the Royal Society and University of Manchester, the National Basic Research Program (nos. 2013CB933402 and 2016YFA0301004), and the National Natural Science Foundation of China (nos. 21527803, 21471009, 21621061, and 21871009) for funding. This project has received funding from the European Research Council (ERC) under the European Union's Horizon 2020 Research and Innovation Programme (grant agreement no. 742401, NANOCHEM). We are grateful to the Diamond Light Source and the STFC/ISIS Facility for access to beamlines B22 and TOSCA, respectively. This research used the resources of beamlines 11.3.1 and 12.2.1 at the Advanced Light Source, which is a DOE Office of Science User Facility under contract no. DE-AC02-05CH11231. The computing resources were made available through the VirtuES and ICE-MAN projects, funded by the Laboratory Directed Research and Development Program and the Compute and Data Environment for Science (CADES) at ORNL. J.L., X.Z., and Z.Z. thank the China Scholarship Council (CSC) for funding.

■ REFERENCES

(1) Kalmutzki, J. M.; Hanikel, N.; Yaghi, M. O. Secondary building units as the turning point in the development of the reticular chemistry of MOFs. *Sci. Adv.* **2018**, *4*, eaat9180.
(2) Bloch, E. D.; Queen, W. L.; Krishna, R.; Zadrozny, J. M.; Brown, C. M.; Long, J. R. Hydrocarbon separation in a metal-organic framework with open iron(II) coordination sites. *Science* **2012**, *335*, 1606.
(3) Schneemann, A.; Bon, V.; Schwedler, I.; Senkovska, I.; Kaskel, S.; Fischer, R. A. Flexible metal-organic frameworks. *Chem. Soc. Rev.* **2014**, *43*, 6062−6096.
(4) Han, X.; Godfrey, H. G. W.; Briggs, L.; Davies, A. J.; Cheng, Y.; Daemen, L. L.; Sheveleva, A. M.; Tuna, F.; McInnes, E. J. L.; Sun, J.; Drathen, C.; George, M. W.; Ramirez-Cuesta, A. J.; Thomas, K. M.; Yang, S.; Schröder, M. Reversible adsorption of nitrogen dioxide within a robust porous metal-organic framework. *Nat. Mater.* **2018**, *17*, 691−696.
(5) Krause, S.; Bon, V.; Senkovska, I.; Stoeck, U.; Wallacher, D.; Többens, D. M.; Zander, S.; Pillai, R. S.; Maurin, G.; Coudert, F.-X.; Kaskel, S. A pressure-amplifying framework material with negative gas adsorption transitions. *Nature* **2016**, *532*, 348−352.
(6) Katsoulidis, A. P.; Antypov, D.; Whitehead, G. F. S.; Carrington, E. J.; Adams, D. J.; Berry, N. G.; Darling, G. R.; Dyer, M. S.; Rosseinsky, M. J. Chemical control of structure and guest uptake by a conformationally mobile porous material. *Nature* **2019**, *565*, 213−217.
(7) Gu, C.; Hosono, N.; Zheng, J.-J.; Sato, Y.; Kusaka, S.; Sakaki, S.; Kitagawa, S. Design and control of gas diffusion process in a nanoporous soft crystal. *Science* **2019**, *363*, 387−391.
(8) Goodwin, A. L.; Calleja, M.; Conterio, M. J.; Dove, M. T.; Evans, J. S. O.; Keen, D. A.; Peters, L.; Tucker, M. G. Colossal positive and negative thermal expansion in the framework material $Ag_3[Co(CN)_6]$. *Science* **2008**, *319*, 794−797.
(9) Serre, C.; Millange, F.; Thouvenot, C.; Noguès, M.; Marsolier, G.; Louër, D.; Férey, G. Very large breathing effect in the first nanoporous chromium(III)-based solids: MIL-53 or $Cr(III)(OH)\cdot\{O_2C\text{-}C_6H_4\text{-}CO_2\}\cdot\{HO_2C\text{-}C_6H_4\text{-}CO_2H\}_x\cdot H_2O_y$. *J. Am. Chem. Soc.* **2002**, *124*, 13519−13526.
(10) Deria, P.; Gómez-Gualdrón, D. A.; Bury, W.; Schaef, H. T.; Wang, T. C.; Thallapally, P. K.; Sarjeant, A. A.; Snurr, R. Q.; Hupp, J. T.; Farha, O. K. Ultraporous, water stable, and breathing zirconium-based metal-organic frameworks with *ftw* topology. *J. Am. Chem. Soc.* **2015**, *137*, 13183−13190.
(11) Sung Cho, H.; Deng, H.; Miyasaka, K.; Dong, Z.; Cho, M.; Neimark, A. V.; Ku Kang, J.; Yaghi, O. M.; Terasaki, O. Extra adsorption and adsorbate superlattice formation in metal-organic frameworks. *Nature* **2015**, *527*, 503−507.
(12) Janssen, T.; Chapuis, G.; Boissieu, M. *Aperiodic Crystals: From Modulated Phases to Quasicrystals: Structure and Properties*; Oxford University Press: Oxford, 2018.
(13) Baerlocher, C.; Weber, T.; McCusker, L.; Palatinus, L.; Zones, I. S. Unraveling the perplexing structure of the zeolite SSZ-57. *Science* **2011**, *333*, 1134−1137.
(14) Lin, X.; Blake, A. J.; Wilson, C.; Sun, X. Z.; Champness, N. R.; George, M. W.; Hubberstey, P.; Mokaya, R.; Schröder, M. A porous framework polymer based on a zinc(II) 4,4′-bipyridine-2,6, 2′, 6′-tetracarboxylate: synthesis, structure, and "zeolite-like" behaviors. *J. Am. Chem. Soc.* **2006**, *128*, 10745−10753.
(15) Petricek, V.; Dusek, M.; Palatinus, L. Crystallographic computing system JANA2006: general features. *Z. Kristallogr. - Cryst. Mater.* **2014**, *229*, 345−352.
(16) Clark, S. J.; Segall, M. D.; Pickard, C. J.; Hasnip, P. J.; Probert, M. I. J.; Refson, K.; Payne, M. C. First principles methods using CASTEP. *Z. Kristallogr. - Cryst. Mater.* **2005**, *220*, 567−571.
(17) Cheng, Y. Q.; Daemen, L. L.; Kolesnikov, A. I.; Ramirez-Cuesta, A. J. Simulation of inelastic neutron scattering spectra using OCLIMAX. *J. Chem. Theory Comput.* **2019**, *15*, 1974−1982.
(18) Boyer, L. L.; Kaxiras, E.; Feldman, J. L.; Broughton, J. Q.; Mehl, M. J. New low-energy crystal structure for silicon. *Phys. Rev. Lett.* **1991**, *67*, 715.
(19) Stokes, H. T.; Hatch, D. M.; Campbell, B. J. ISO(3+d)D, *ISOTROPY Software Suite*, iso.byu.edu.
(20) Brese, N. E.; O'Keeffe, M. Bond-valence parameters for solids. *Acta Crystallogr., Sect. B: Struct. Sci.* **1991**, *47*, 192−197.
(21) Ovsyannikov, S. V.; Bykov, M.; Bykova, E.; Kozlenko, D. P.; Tsirlin, A. A.; Karkin, A. E.; Shchennikov, V. V.; Kichanov, S. E.; Gou, H.; Abakumov, A. M.; Egoavil, R.; Verbeeck, J.; McCammon, C.; Dyadkin, V.; Chernyshov, D.; van Smaalen, S.; Dubrovinsky, L. S. Charge-ordering transition in iron oxide Fe_4O_5 involving competing dimer and trimer formation. *Nat. Chem.* **2016**, *8*, 501−508.
(22) Prokeš, K.; Hartwig, S.; Gukasov, A.; Mydosh, J. A.; Huang, Y. K.; Niehaus, O.; Pöttgen, R. Coexistence of different magnetic moments in CeRuSn probed by polarized neutrons. *Phys. Rev. B: Condens. Matter Mater. Phys.* **2015**, *91*, 014424.
(23) Sun, Z.; Li, J.; Ji, C.; Sun, J.; Hong, M.; Luo, J. Unusual long-range ordering incommensurate structural modulations in an organic molecular ferroelectric. *J. Am. Chem. Soc.* **2017**, *139*, 15900−15906.

(24) He, H.; Tan, X. Electric-field-induced transformation of incommensurate modulations in antiferroelectric $Pb_{0.99}Nb_{0.02}[(Zr_{1-x}Sn_x)_{1-y}Ti_y]_{0.98}O_3$. *Phys. Rev. B: Condens. Matter Mater. Phys.* **2005**, *72*, 024102.
(25) Cui, X.; Yang, Q.; Yang, L.; Krishna, R.; Zhang, Z.; Bao, Z.; Wu, H.; Ren, Q.; Zhou, W.; Chen, B.; Xing, H. Ultrahigh and selective SO_2 uptake in inorganic anion-pillared hybrid porous materials. *Adv. Mater.* **2017**, *29*, 1606929.
(26) Yang, S.; Liu, L.; Sun, J.; Thomas, K. M.; Davies, A. J.; George, M. W.; Blake, A. J.; Hill, A. H.; Fitch, A. N.; Tang, C. C.; Schröder, M. Irreversible network transformation in a dynamic porous host catalyzed by sulfur dioxide. *J. Am. Chem. Soc.* **2013**, *135*, 4954−4957.
(27) Yang, S.; Sun, J.; Ramirez-Cuesta, A. J.; Callear, S. K.; David, W. I. F.; Anderson, D. P.; Newby, R.; Blake, A. J.; Parker, J. E.; Tang, C. C.; Schröder, M. Selectivity and direct visualization of carbon dioxide and sulfur dioxide in a decorated porous host. *Nat. Chem.* **2012**, *4*, 887−894.
(28) Bell, J. G.; Morris, S. A.; Aidoudi, F.; McCormick, L. J.; Morris, R. E.; Thomas, K. M. Physisorption-induced structural change directing carbon monoxide chemisorption and nitric oxide coordination on hemilabile porous metal organic framework $NaNi_3(OH)(SIP)_2(H_2O)_5{\cdot}H_2O$ (SIP = 5-sulfoisophthalate). *J. Mater. Chem. A* **2017**, *5*, 23577−23591.
(29) Dubbeldam, D.; Calero, S.; Maesen, T. L. M.; Smit, B. Incommensurate diffusion in confined systems. *Phys. Rev. Lett.* **2003**, *90*, 245901.
(30) Banerjee, D.; Wang, H.; Gong, Q.; Plonka, A. M.; Jagiello, J.; Wu, H.; Woerner, W. R.; Emge, T. J.; Olson, D. H.; Parise, J. B.; Li, J. Direct structural evidence of commensurate-to-incommensurate transition of hydrocarbon adsorption in a microporous metal organic framework. *Chem. Sci.* **2016**, *7*, 759−765.
(31) Han, X.; Yang, S.; Schröder, M. Porous metal-organic frameworks as emerging sorbents for clean air. *Nat. Rev. Chem.* **2019**, *3*, 108−118.
(32) Wu, W.; Han, B.; Gao, H.; Liu, Z.; Jiang, T.; Huang, J. Desulfurization of flue gas: SO_2 absorption by an ionic liquid. *Angew. Chem., Int. Ed.* **2004**, *43*, 2415−2417.
(33) Zheng, D.; An, Y.; Li, Z.; Wu, J. Metal-free aminosulfonylation of aryldiazonium tetrafluoroborates with $DABCO{\cdot}(SO_2)_2$ and hydrazines. *Angew. Chem., Int. Ed.* **2014**, *53*, 2451−2454.

https://dx.doi.org/10.1021/jacs.0c08794
J. Am. Chem. Soc. 2020, 142, 19189−19197